ACS Catalysis

Research Article

pubs.acs.org/acscatalysis

Promotional Effect of the Base Metal on Bimetallic Au−Ni/CeO_2 Catalysts Prepared from Core−Shell Nanoparticles

Juan P. Holgado,* Fatima Ternero, Victor M. Gonzalez-delaCruz, and Alfonso Caballero

Instituto de Ciencia de Materiales de Sevilla y Departamento de Química Inorgánica, CSIC-Universidad de Sevilla, Avenida Américo Vespucio, 49, 41092 Sevilla, Spain

Supporting Information

ABSTRACT: A set of three catalysts (a Au−Ni bimetallic and their corresponding Au and Ni monometallics) has been prepared by impregnation of previously prepared suspensions of monodisperse metallic particles to ensure the precise control of their physicochemical characteristics (size and composition). The Au−Ni/CeO_2 bimetallic catalysts present better reactivity toward CO oxidation than monometallic Au/CeO_2 and Ni/CeO_2 prepared under identical conditions. "operando-like" characterization of Ni and Au atoms into the bimetallic particles using, among other techniques, ambient-pressure photoelectron spectroscopy and diffuse reflectance infrared Fourier transform spectroscopy has allowed us to determine that under oxidative conditions the samples present a Au@NiO core−shell distribution, where Ni surface atoms are affected by an electronic effect from inner Au atoms.

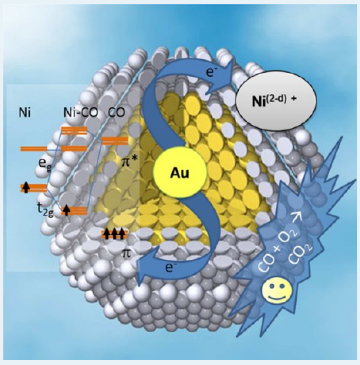

KEYWORDS: *heterogeneous catalysis, nanoparticles, gold bimetallics, electronic effect, synergy, atom economy*

INTRODUCTION

Since the seminal work of Haruta,[1] myriad papers describing the preparation of gold nanoparticles onto different supports have been published in the past two decades. Most of these papers have focused, because of the good characteristics of the catalysts so prepared, on the preparation of gold particles from a solution containing Au^{3+} ions (typically as $AuCl_4^-$) and its adsorption or deposition onto a support added in this solution (in the form of a solid suspension). Nevertheless, some other techniques such as wetness impregnation, electrochemical synthesis, photochemical reduction,[2−4] etc., have been also studied.

An alternative to these "traditional" methods arises with blossoming of synthesis recipes for gold colloid nanoparticles (NPs). Colloid preparation techniques provide metal particles with well-defined size or structure (i.e., shape and thus faces exposed) without other perturbations, but at the same time, simple changes in the recipes allow a significant variation of those parameters. This homogeneity and tunability of the metal nanoparticle properties make the NPs so obtained excellent materials that are suitable for catalytic investigations.[5] The intensive research, over the past decade, on liquid phase synthesis of metal nanostructures has resulted in the development of reproducible methods for the preparation of nanocrystals with controlled size and shape (and composition in the case of bimetallics), in quantities and qualities suitable for the preparation of catalysts (at least at lab scale) that allow meaningful studies of the relationship of their size, shape, and composition with their reactivity.

As exposed in the recent reviews of Rossi,[6] Corma,[7] and Hutchings,[8] among others, the development of gold bimetallic catalysts yields beneficial aspects, such as a high stability against oxygen and a tolerance to chemical groups such as aliphatic and aromatic amines, a higher selectivity (compared with that of Pt group metals), and an ability to discriminate within chemical groups and geometrical positions. One extra reason for this interest is the economic benefit if the second metal is much cheaper than gold. Among some other metals, the use of base metals such as Cu or Ni results in an increasing number of publications. At this point, it is again interesting to note that with the use of colloidal techniques it is possible to prepare nanoparticles with a controlled size and composition but also to allow, in most of the cases, a desired metal distribution inside the particle to be obtained (pseudo alloy, cluster in cluster, or core@shell). Therefore, if an appropriate method could be found to deposit these colloidal nanoparticles onto a support without largely affecting their original properties, we could have a method for obtaining "tailor-made" catalysts and, hence, a way to correlate different physicochemical properties with their catalytic activity.

In this context, it has been found that bimetallic systems of interest to catalysis are not limited to combinations of metallic elements that are highly miscible in the bulk. For instance, the bulk binary phase diagram of Au and Ni has a large miscibility gap, and no alloy is formed at low temperatures. However, it has been found by STM and theoretical calculations,[9,10] that the formation of a surface alloy of Au on Ni(110) and Ni(111) is energetically favorable. This formation of an alloy of Au on

Received: October 29, 2012
Revised: July 18, 2013
Published: July 26, 2013

   dx.doi.org/10.1021/cs400293b | ACS Catal. 2013, 3, 2169−2180

the surface of a Ni would influence the chemical and reactivity properties of such particles, with a downshift in the local density of Ni d states because of the presence of neighboring Au atoms.[11,12]

Here, we have studied a set of three catalysts (a Au−Ni bimetallic and their corresponding Au and Ni monometallics) prepared by impregnation of previously prepared suspensions of monodisperse metallic particles to compare the effect of addition of Ni to gold nanoparticles on catalytic activity. In this context, research on bimetallic clusters has traditionally lacked suitable physical methods, and the study of such systems was mainly achieved with catalytic activity tests. With the development of synchrotron techniques, such as X-ray absorption, researchers have gained tools that are particularly well suited for the investigation of highly disperse bimetallic clusters, and important results with respect to their catalyst structure have been described. Here we have studied the "operando-like" distribution of Ni and Au atoms in bimetallic particles using, diffuse reflectance infrared Fourier transform spectroscopy (DRIFTS), ambient-pressure photoelectron spectroscopy (APPES), X-ray absorption near edge structure (XANES), and other conventional techniques.

It is well-known that supported Au NPs are extraordinarily active in CO oxidation, especially with supports such as TiO_2 and CeO_2. Thus, Au/TiO_2 and Au/CeO_2 have proven to be much more active than other noble metal catalysts at temperatures below 400 K. Recently,[13] the temperature range in which the activity for CO oxidation is observed has been extended to 70 K by using a Au−Ni alloy. Therefore, we have chosen this reaction as a simple but "probe" test for correlating reactivity data of samples prepared here with the effects of incorporation of Ni atoms into gold nanoparticles.

EXPERIMENTAL SECTION

Preparation of Nanoparticles. All reactants were used as received from the suppliers (Alfa, Aldrich, and Fluka) and were at least 99% pure.

Au, Ni, and Au−Ni NPs were prepared by a slight modification of a recipe described previously[14] based on the reduction of metal complex method. Basically, 4 mmol of metal salt was dissolved in 10 mL of diphenyl ether (flask A), and then the mixture was heated at 353 K, purged under vacuum, and then submitted to a flow of bubbling N_2. In a separate flask (flask B), 40 mL of diphenyl ether and typically 4 mmol of oleic acid and tri-*n*-octylphospine (TOP) were heated at ∼500 K. At this temperature, the solution in flask B containing the metallic salts was rapidly injected into flask A, causing the decomposition of the precursor salt, followed by nucleation and growth of metallic nanoparticles. As long discussed,[15,16] the type and concentration of both reductor and surfactant (although also reaction time and temperature) control the resulting particle size of the NPs. After this preparation procedure, NPs were separated from the rest of the reactants by centrifugation (adding ethanol to induce precipitation and coalescence of NPs). Precipitated NPs were further dispersed again in *o*-dichlorobenzene and purified several times using the precipitation method, being, for the purpose of storage, suspended in *o*-dichlorobenzene and oleic acid.

Preparation of Catalysts. Au/CeO_2, Ni/CeO_2, and $Au-Ni/CeO_2$ catalysts were prepared by impregnation of a suspension of Au, Ni, and Au−Ni nanoparticles (in *o*-dichlorobenzene and oleic acid) onto a commercial high-surface area cerium oxide (CeO_2, HSA-20, from RODIA) using a method similar to that of impregnation at incipient wetness (preparation of Au, Ni, and Au−Ni NPs is described above). After deposition of the NPs, the catalysts were dried overnight in an oven at 400 K and then crushed in an agatha mortar. Finally, the solids were calcined in an O_2 (3%)/He mixture at 773 K. That temperature was set after a control experiment in which we checked that the decomposition of organic compounds from the suspension solvent had been completed.

Scanning Electron Microscopy (SEM) and X-ray Diffraction (XRD). SEM images were obtained in a Hitachi S-4800 FEGSEM microscope, with a field emission filament, using an accelerating voltage of 2−5 kV and an extraction current of 10 μA. For STEM (transmitted electrons) images, the voltage was set at 30 kV. X-ray diffractograms were recorded with Siemens D-500 equipment, with a Bragg-Brentano configuration, using Cu Kα radiation (λ = 1.5418 Å), and a scan range 2θ of 20−80°, with a step of 0.033° and an acquisition time of 100 s for each point.

Temperature-Programmed Reduction (TPR). Temperature-programmed experiments were conducted according to the experimental conditions described elsewhere to avoid the coalescence of peaks.[17] An amount of sample that would consume approximately 100 μmol of H_2 was used in all cases. A H_2/Ar mixture (5% H_2, flow rate of 10 mL/min) was used as the reducing atmosphere, from room temperature to 1173 K, with a heating rate of 10 K/min. A thermal conductivity detector (TCD), previously calibrated using CuO, and a mass spectrometer in line with the TCD, calibrated with reference mixtures, were used to detect variations in H_2 concentration and monitor possible subproduct formation.

Catalytic Activity Tests. The reaction was conducted in a tubular reactor (U-shaped), using 35 mg of catalysts between two pompons of quartz wool. Mixtures of gases consisted of CO (1 vol %) diluted in He and a molar equivalent of O_2 (1/3). Au/CeO_2, Ni/CeO_2, and $Au-Ni/CeO_2$ catalysts in contact with the reaction mixture were heated from room temperature to 573 K at a rate of 2.0 K/min and cooled to room temperature in the same reaction mixture. All the samples were in contact with a flow of pure He (50 mL/min) for 30 min prior to contact with the reactant mixture. Although no steady state measurements were taken, the stability of catalysts was checked repeating the reaction measurement cycle at least twice. In all the cases, the results showed a reproducibility for each point of ∼1−2%. An example of such reproducibility tests has been incorporated into the Supporting Information. Reactives and products were analyzed using a mass spectrometer and a gas chromatograph (Varian, GC-3800) equipped with a thermal conductivity detector (TCD) and two columns with an "in line" configuration (Molecular Sieve 5 Å, Porapak-N).

X-ray Absorption Spectroscopy (XAS). X-ray absorption spectra were recorded at the SuperXAS beamline of the SLS synchrotron (Villigen, Switzerland) and BM-25 beamline of the ESRF synchrotron (Grenoble, France). The spectra were all acquired in transmission mode, the pellets being prepared using the optimal weight to maximize the signal-to-noise ratio in the ionization chambers ($\log I_0/I_1 \approx 1$) and mixed with BN if needed. For energy calibration, a Ni or Au foil was introduced after the ionization chamber (I_1) and measured simultaneously. Typical XAS spectral K edges were recorded from 8230 to 9190 eV (Ni K edge) or from 11900 to 12900 eV (Au L-III edge), with a variable step energy value and a minimum step of 0.5 eV across the XANES region.

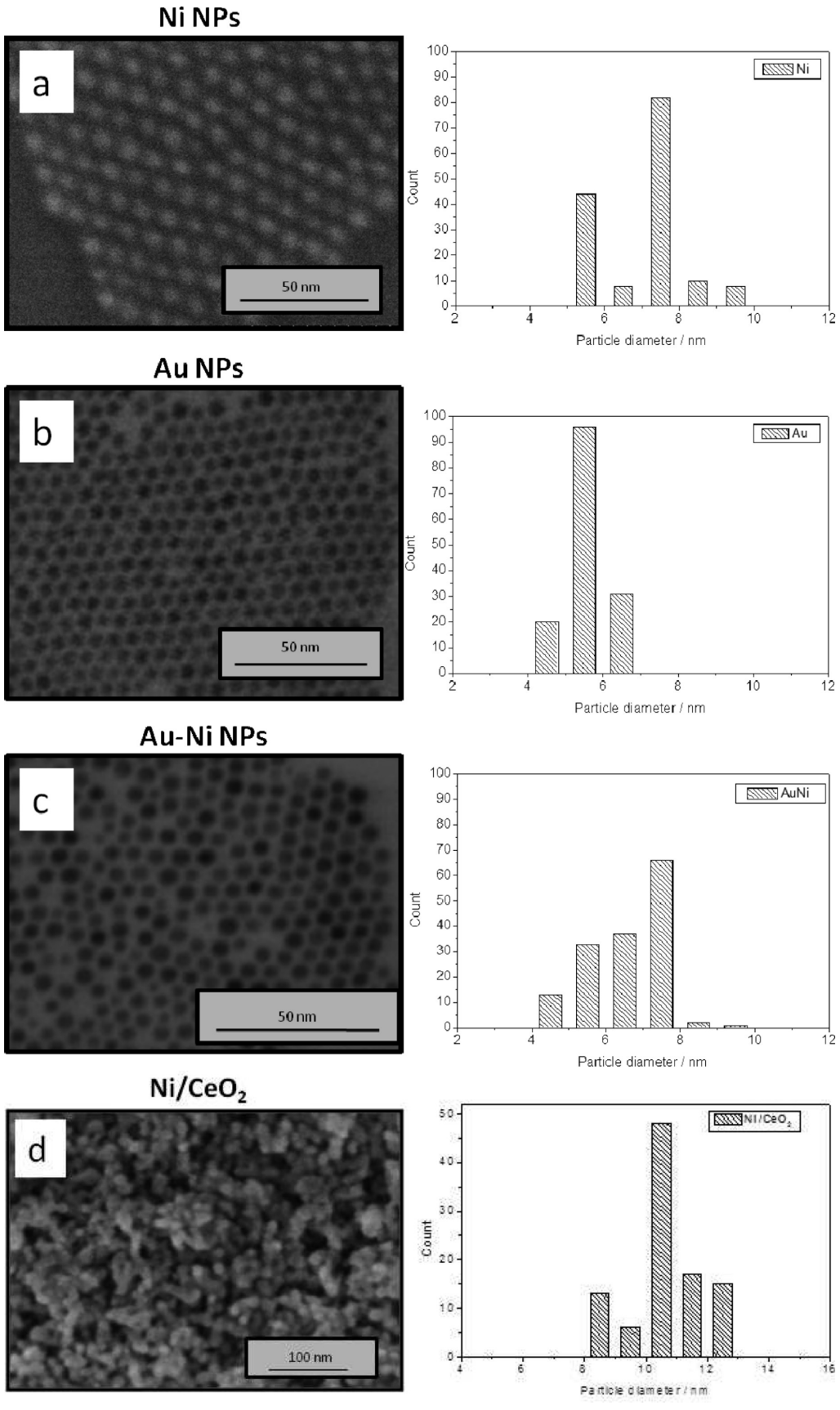

Figure 1. continued

dx.doi.org/10.1021/cs400293b | *ACS Catal.* 2013, 3, 2169−2180

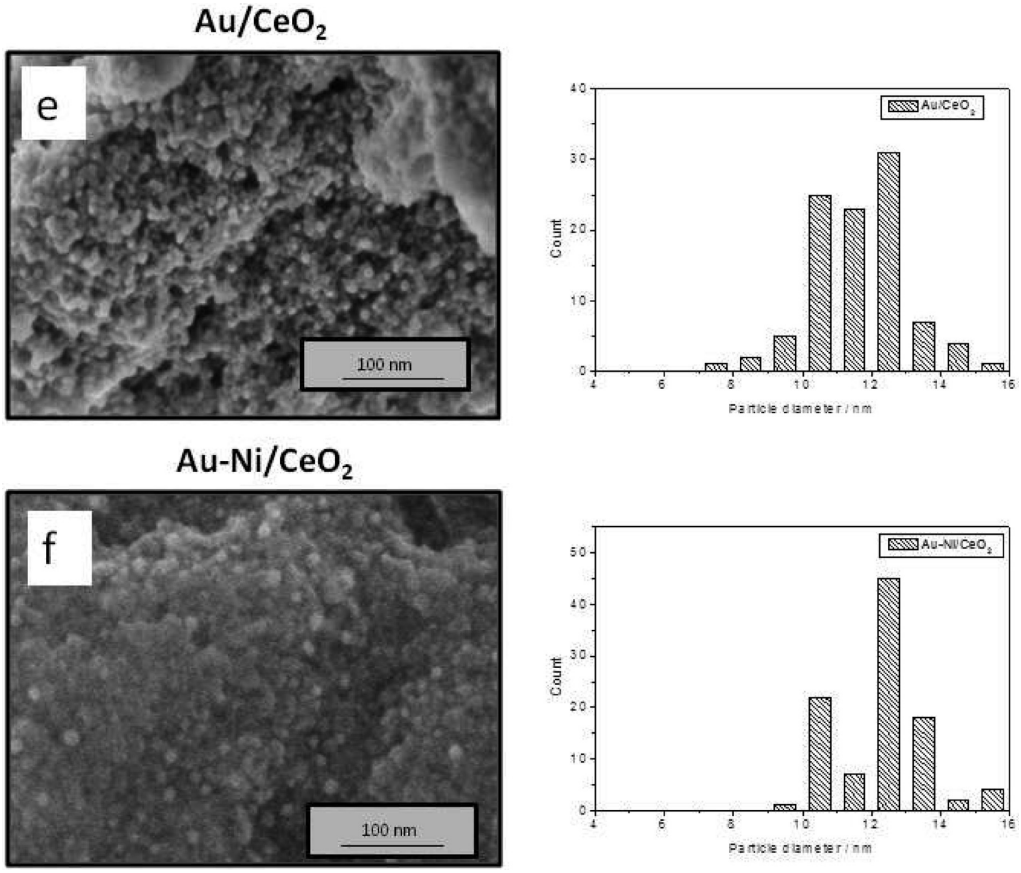

Figure 1. TEM images (left) of (a) Ni, (b) Au, and (c) Au−Ni nanoparticles before nanoparticle impregnation and calcination and histograms (right) of the size distribution for metal particles obtained from TEM images. SEM images (left) of (d) Ni/CeO_2, (e) Au/CeO_2, and (f) $Au–Ni/CeO_2$ catalysts after nanoparticle impregnation and calcination and histograms (right) of the size distribution for metal particles obtained from SEM images.

DRIFTS. FTIR spectra were recorded in a FTIR JASCO 6300 instrument equipped with a "Praying Mantis" DRIFTS cell, using a reaction chamber able to work up to 873 K under a controlled atmosphere. Mass flow controllers were utilized for dosing the gases to the chamber, passing through the powder sample. FTIR spectra were collected in the range of 4000−700 cm^{-1} with a resolution of 4 cm^{-1} and 100 scans each. Spectra were acquired at room temperature during the "in situ" treatment with a partial pressure of CO (~8 Torr) and after the sample had been purged with helium for 20 min.

X-ray Photoelectron Spectroscopy (XPS) and Ambient-Pressure Photoelectron Spectroscopy (APPES). Conventional XPS measurements were taken on pelletized samples mounted on a stainless steel sample holder, after evacuation up to ultra high vacuum ($P < 2 \times 10^{-9}$ mbar) at room temperature using a nonmonochromatized dual X-ray source, with a hemispherical analyzer (SPECS Phoibos 100) working in fixed transmission mode with a 20 eV pass energy resolution.

In situ XPS experiments were conducted at beamline U49/2-PGM1 at BESSY (Berlin, Germany). This setup operates like the instrument described elsewhere.[18−20] Basically, the sample can be studied under a gas mixture (in the millibar region), minimizing the possible scattering of photoelectrons through the gas phase. This is done placing the sample in front of a differentially pumped electrostatic lens and only 1−2 mm in front of the first aperture of such a lens system. The surface normal of the sample is parallel to the optical axis of our lens system, and incidence X-rays irradiate the sample at an angle of <55° from the surface normal.

A pressed pellet of catalyst containing ~100 mg of $Au–Ni/CeO_2$ catalyst was activated in situ in oxygen (0.5 mbar, 573 K) and then submitted to the indicated treatments. Gas flow (22−32 N mL/min) into the reaction cell was adjusted using calibrated mass flow controllers and leak valves. Gas phase analysis was performed with a quadrupole Balzers mass spectrometer connected to the experimental cell through a leak valve. Ce 3d, O 1s, Ni 2p, and Au 4f spectra were recorded with appropriate photon energies to give always photoelectrons of 200 and 600 eV, for mentioned regions. The binding energies were calibrated using internal references, such as the Ce 3d u‴ (917.0 eV) states.[21] The energy calibration was necessary because surface charging occurred because of the emission of photoelectrons, although the calibration applied was always in the range of 1−3 eV.

It is worth mentioning that during the setup of the APPES, there were some doubts about the convenience of using CO in the presence of Ni, because of the possible formation of volatile Ni carboniles that would contaminate the chamber. Because reaction tests were conducted in a mixture of CO and O_2 (with excess O_2) and we sought to avoid the CO in the mixture, we decided to conduct the experiment under (a) oxidizing conditions (O_2, ~1 mbar) and (b) reducing conditions (H_2 instead of CO, also a reductant, ~1 mbar).

dx.doi.org/10.1021/cs400293b | ACS Catal. 2013, 3, 2169−2180

RESULTS

Figure 1 shows TEM images of Au, Ni, and Au/Ni bimetallic nanoparticles. As one can observe, in all cases, the images show particles that probably correspond with spherical shapes (although a polyhedral shape could not be excluded), well formed, with a size very similar in all cases (6 nm) and a narrow size distribution. In fact, a detailed statistical analysis (see Figure 1, right) performed via an "in house" software image analysis of more than 150 individual particles reveals that more than 60% of the particles have a size of 6−8 nm and 90% of them are inside a range of 6 ± 2 nm. Chemical analysis of these NPs, performed by inductively coupled plasma atomic emission spectroscopy (ICP-AES), reveals also the monometallic composition of Au and Ni NPs and the bimetallic character (with an atomic Au/Ni ratio of 1/0.85) of the Au−Ni NPs.

As explained and detailed in Experimental Section, these NPs were maintained in *o*-dichlorobenzene and deposited into a high-surface area CeO_2 (HSA-20, RODIA), using a method similar to classical impregnation at incipient wetness. After deposition and calcination at 773 K, samples were analyzed by atomic absorption, confirming that in the three catalysts the loading was ∼3% (atomic) ± 0.5%, confirming the intended preparation parameters. An analysis of TEM and SEM images, similar to that employed for the NPs, allowed us to calculate the mean size of metallic particles after their deposition onto the CeO_2 support. That analysis resulted in a value of ∼10−12 nm, indicating a partial sintering of NPs (see the Supporting Information). Nevertheless, it must be stated that the statistical analysis showed also a very narrow distribution of the particles in the catalyst after deposition and calcination.

Complete removal of capping is a key issue in the works of supported nanoparticles, especially in those involving catalytic studies. We have conducted several studies that are presented in the Supporting Information to clarify this point. First, we have run an elementary analysis (C, N, and H, using a LECO TruSpec CHN instrument) for one of the uncalcined and calcined samples. The data show that the calcination process decreases the amount of carbon by a factor of almost 100. We conducted a temperature-programmed oxidation (TPO) experiment, in which CO_2 formation is followed by mass spectrometry versus temperature under a synthetic air flow. We found that the carbon dioxide signal presents a peak below 500 °C and that above that temperature no more CO_2 was formed (Figure 2 of the Supporting Information). Finally, we also compared XPS of three samples: uncalcined sample, calcined "ex situ", and calcined in situ. With respect to the uncalcined sample, the carbon content is decreased in the sample calcined, by a factor of ∼20. More importantly, the carbon signal was almost absent when the sample was calcined in situ in a conventional XPS system equipped with a high-temperature cell (Figure 3a of the Supporting Information). A similar result was also obtained with the APPES experiment, where the initial carbon signal disappeared after the sample had been heated in oxygen at 673 and 773 K. The latter result is especially significant, as it was taken with a kinetic energy of photoelectrons (200 eV) that enhances the surface sensitivity (Figure 3b of the Supporting Information). Both results, from conventional XPS and APPES, indicate that the residual carbon signal found in the sample calcined ex situ is adventious carbon coming from exposure to atmosphere and indicate clearly that the calcination treatment led to a sample with no significant carbon that could modify the reactivity. Although Ni 2p and Au 4f signals are relatively weak, the XPS data and the chemical analysis allowed us to confirm that the metallic phase was mainly deposited into the surface of CeO_2 agglomerates, because Ni 2p and Au 4f signals were stronger than those expected for a homogeneous distribution. This apparent small signal could be the result of several factors. First, particles are relatively large (12 nm), which correlates with a dispersion of ∼8%. Second, in particulate systems, such as heterogeneous catalysts, is well-known that the signal of the metallic particles (vs support) depends not only on the dispersion of those particles but also on the relative size versus the support particles, and the (meso)porosity of the support.[22] The model used for XPS analysis of the distribution of metal nanoparticles[22] on CeO_2 agglomerates is a semiquantitative model, conceived in relation to problems of catalyst characterization but also other composite or powder materials, in which one of the phases is highly dispersed in the matrix or on the surface of a carrier support. Basic parameters used in the model are the specific surface of the support, the size of the particle of the dispersed phase, and the surface concentration of atoms of the dispersed phase referred to the surface of the support. In brief, the model assumes a close packing of spheres of the support where cubic particles of the dispersed phase are deposited on the external support. On the basis of that model, deviations from the calculated ratio of intensities (dispersed phase/support) can be interpreted as a surface segregation or its preferential distribution into the pores of the support. According to data obtained from that model, some of the Ni particles could be located on that mesoporous form and would not contribute to the Ni 2p signal but would be still accessible for gases. Besides this fact, conventional XPS results are discussed further in the text in more detail (Figure 7)

XAS (XANES) spectra have been recorded for a calcined and reduced Au−Ni/CeO_2 sample (see Figure 2). Au L_{III} XANES

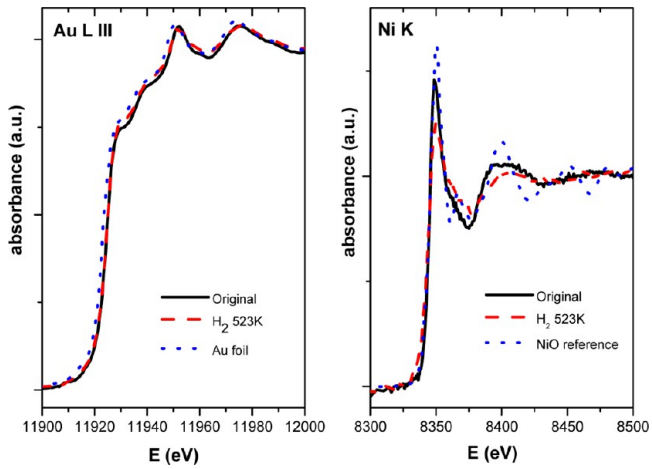

Figure 2. XANES spectra of the Au−Ni sample after calcination at 773 K and reduction at 523 K, corresponding to Au L-III and Ni K edges. Spectra for NiO and Au^0 have been incorporated as references.

of the Au−Ni/CeO_2 sample reflects a spectrum almost coincident with that of a gold reference; Ni K edge XANES reflects mostly the shape of a Ni^{2+} reference, but there is a decrease in the intensity of the "white line". These changes are more accentuated after reduction at 523 K. This decrease in the intensity of the white line could be reflecting, among some other effects, a change in the electronic density of Ni^{2+}, because those changes in the intensity of this feature have been

dx.doi.org/10.1021/cs400293b | ACS Catal. 2013, 3, 2169−2180

traditionally associated with changes in the population of the occupied d orbitals of the transition metal. In fact, in the work of Chin et al.,[23] the authors report that at low Au loadings of Au−Ni/MgO−Al_2O_3 catalysts (0.2% Au and 8.8% Ni), the XANES features of both the Ni K edge and the Au L_{III} edge are affected, with changes in the intensity of the white lines that reflect an electronic transfer from Au atoms toward the (oxidized) Ni atoms. XRD data, included in Figure 3, provide

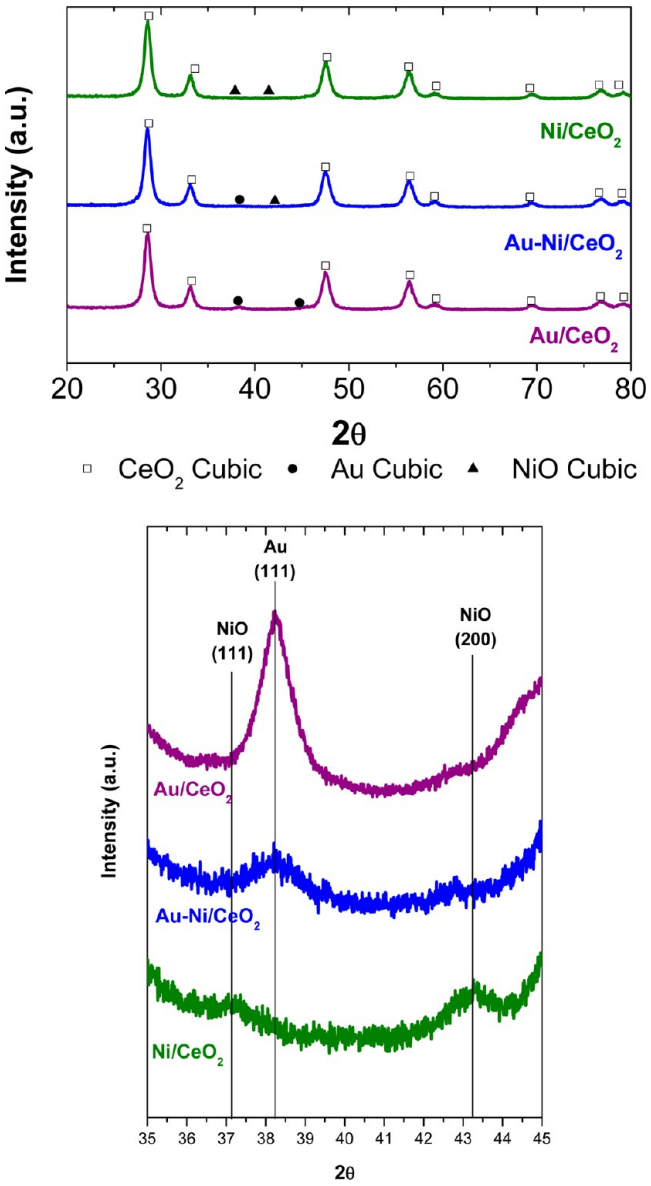

Figure 3. XRD data of calcined Au/CeO_2, Ni/CeO_2, and Au−Ni/CeO_2 catalysts. The inset shows the magnification of the zone for Au(111) and Ni(111) peaks.

additional information. Thus, while Au(111) peaks are observed in the Au/CeO_2 and Au−Ni/CeO_2 samples, no nickel peaks (neither NiO nor Ni^0) are detected in the Ni/CeO_2 or Au−Ni/CeO_2 samples. It is also interesting to note that in the Au−Ni/CeO_2 sample there is significant decrease in the intensity of the Au(111) peak, giving a value much lower than expected for 50% of gold atoms with respect to the Au/CeO_2 sample. This could reflect a more amorphous distribution of Au and Ni atoms in the bimetallic samples, maybe because of a smaller nanocrystalline or more random distribution of these atoms.

Programmed Temperature Reduction (TPR). TPR profiles of the M/CeO_2 (M = Au, Ni, and Au−Ni) samples are plotted in Figure 4, including that of CeO_2 used as a

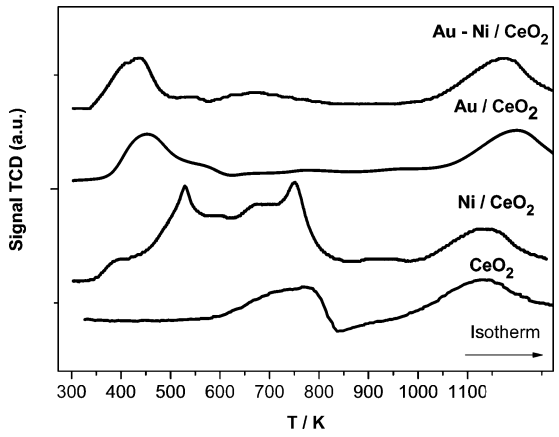

Figure 4. TPR profiles of the M/CeO_2 samples (M = Au, Ni, and Au−Ni), including the profile of the CeO_2 used as a support as a reference.

support as a reference. The latter profile presents two broad peaks centered at ∼780 and ∼1050 K, which have been long discussed and normally assigned to surface and bulk reduction at CeO_2 particles.[24,25] As one can observe, the CeO_2 "bulk" reduction peak remains almost unchanged in all the catalysts with respect to the CeO_2 support. This is consistent with similar results for M/CeO_2 samples.[26,27] Therefore, this peak will not be discussed in more detail. It is important to note that the amount of hydrogen consumption in the surface reduction process (for the CeO_2 here used) is ∼450 μmol/g of CeO_2, a value that will be used for comparison with those of the M/CeO_2 samples.

For M/CeO_2 samples, it has been reported[28,29] that reduction of the metallic phase from its oxidized state and surface reduction of CeO_2 particles usually take place almost simultaneously, normally with a shift to lower temperatures with respect to MO_x and CeO_2 pure phases. In the case of the Ni/CeO_2 sample, several superposed peaks are observed with maxima at 523, 673, and 753 K. In fact, although some of the peaks observed for the Ni/CeO_2 sample could be assigned to the reduction of NiO, it is also clear that the reduction process for the CeO_2 surface has been shifted to lower temperatures and probably is included in the broad observed signal. In fact, the amount of hydrogen surface consumption is slightly greater than that corresponding to reduction of NiO and CeO_2, which supports the simultaneous occurrence of both processes.

On the other hand, in the case of the Au/CeO_2 sample only a peak in the low-temperature zone (<773 K) is observed. Quantification of this peak reveals an amount of H_2 consumption of ∼500 μmol/g. Taking into account that all the results indicate that Au is almost in the zero oxidation state, this peak should correspond to the support surface reduction of CeO_2 particles, although the peak shifted from ∼773 to ∼423 K. This effect has been previously observed in other M/CeO_2 systems[30−32] and has been always explained in terms of spillover of H atoms from the metallic particle (Au^0) onto the CeO_2 support.

The profile of the Au−Ni/CeO_2 sample is similar to that of the Au/CeO_2 sample, showing only a peak at ∼423 K, with a

dx.doi.org/10.1021/cs400293b | ACS Catal. 2013, 3, 2169−2180

slightly higher intensity (equivalent to an amount of H_2 consumption of ~600−700 μmol/g). This can be understood following the explanation given for the Au/CeO_2 sample, in terms of H_2 spillover. In the case of the Au/CeO_2 sample, the surface reduction peak of CeO_2 has moved ~300 K. In this case, Au atoms are already reduced in the calcined sample, and the reduction proceeds at the temperature at which spillover takes place over the Au^0 atoms. For the $Au-Ni/CeO_2$ sample, the situation is similar, but now the peak involves both the surface CeO_2 reduction process and reduction of Ni^{2+} to Ni^0. This is why the reduction of the $Au-Ni/CeO_2$ sample seems to be too similar to that of the Au/CeO_2 sample. Spillover of hydrogen atoms onto the Au atoms is the rate-limiting step of the reduction. Nevertheless, please note that this explanation is only feasible if we consider that we may have some Au atoms on the surface, as detected by DRIFTS (see below) and proposed by some authors on the basis of density functional theory (DFT) calculations.

Reactivity Data for CO Oxidation. Figure 5 shows the conversion curves for CO oxidation obtained for the M/CeO_2 samples. In all cases, the total CO conversion is obtained and conversion curves showed a typical sigmoidal curve, where the point of 50% conversion (T_{50}) is usually taken as a reference for the purpose of comparison.

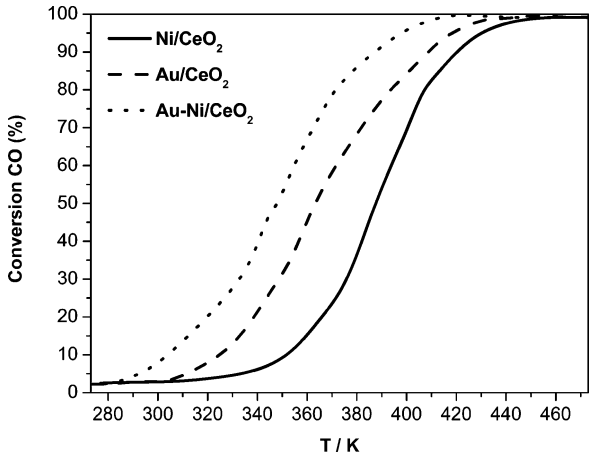

Figure 5. Conversion curves for CO oxidation obtained for the M/CeO_2 samples (0.035 g of catalyst). CO and O_2 reactants were mixed diluted in He at a volume ratio of 1/3/96. GHSV = 3×10^5 L kg^{-1} h^{-1}.

The Ni/CeO_2 sample exhibits a higher T_{50} (388 K), showing a poor reactivity. On the other hand, the Au/CeO_2 exhibits a lower T_{50} (358 K), as expected for this type of catalyst and CO oxidation. It is important here to note that the T_{50} values observed for these catalysts are not especially low, compared with those of similar catalysts, where Au particles are much smaller. Nevertheless, because our study has been performed for the purpose of comparison, and all the samples have similar particle sizes, reactivity can be assumed to be related to chemisorptive interaction between CO and/or O_2 and the metallic particles (and the support).

In this context, the $Au-Ni/CeO_2$ catalyst shows a T_{50} shifted to a temperature lower than that of Au/CeO_2 (348 K). This fact is quite important because in this catalyst we have only 50% of the gold atoms, but a particle size similar to those of Au/CeO_2 and Ni/CeO_2. Besides the economic benefit of this bimetallic sample, this improved reactivity is reflecting some type of synergic interaction between the Ni and Au atoms. Nevertheless, more data about the distribution of Au and Ni atoms in the particle are needed to fully ascribe that synergistic effect.

DRIFTS. The catalyst surface composition was evaluated using DRIFT spectroscopy of adsorbed CO. The DRIFTS spectrum of CO on the Au/CeO_2 catalyst, shown in Figure 6,

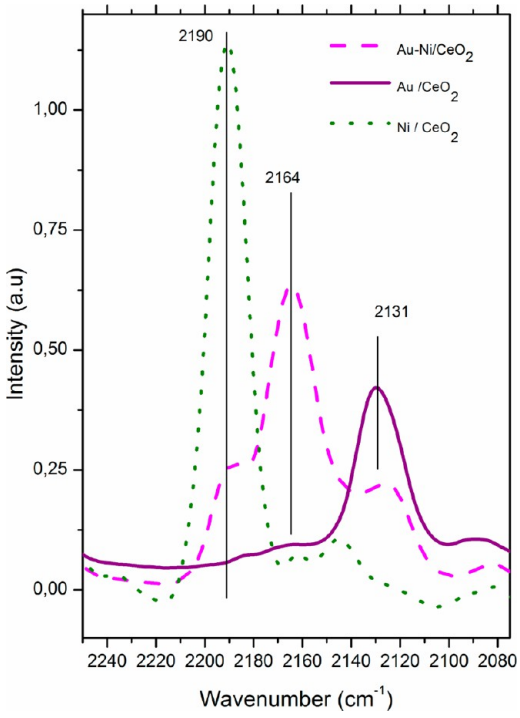

Figure 6. DRIFTS spectra corresponding to calcined M/CeO_2 samples (M = Au, Ni, and Au−Ni), after exposure to CO (8 mbar partial pressure) at room temperature for 20 min (only the CO−metal stretching band zone is shown for the sake of clarity).

contains a single peak at 2131 cm^{-1}. The position of this peak is concordant with those reported in the literature for CO adsorbed on surface Au^0 atoms.[33] The spectrum of the Ni/CeO_2 sample also shows a peak at 2190 cm^{-1}. This position can be attributed to CO adsorbed on cationic Ni^{2+}.[34] On the other hand, the spectrum of the Au−Ni sample presents a major peak, centered at 2164 cm^{-1} with shoulders at 2190 and 2131 cm^{-1} (those later would correspond to the adsorption of CO onto surface Au^0 and Ni^{2+} atoms). These minor shoulders at 2131 and 2190 cm^{-1} should be related to some contributions coming from stretching bands of CO adsorbed on Au^0 and Ni^{2+} atoms. It is important to mention that the presence of some Au^0 atoms could help to explain the observed TPR profile (see above). The position of the main band in the Au−Ni samples, at 2167 cm^{-1}, is completely different from that observed by other authors in bimetallic Au−Ni samples,[35] where only the peaks corresponding to Au^0 (at ~2131 cm^{-1}) and Ni^{2+} (at ~2190 cm^{-1}) were present. In addition, it is important to mention that the position found is not consistent with either $CO-Ni^0$ (bands appearing well below 2100 cm^{-1})[34] or $CO-Au^{3+}$ (found below 2143 cm^{-1}),[36] but furthermore, these species have not been detected by XANES or conventional XPS. One possible assignment would be the formation of $CO-Ni^+$ bands. Although the oxidation state of Ni^+ is not "typical" of nickel, these ions have been detected by FTIR on supported nickel catalysts. The absorption bands of linear $CO-Ni^+$

dx.doi.org/10.1021/cs400293b | ACS Catal. 2013, 3, 2169−2180

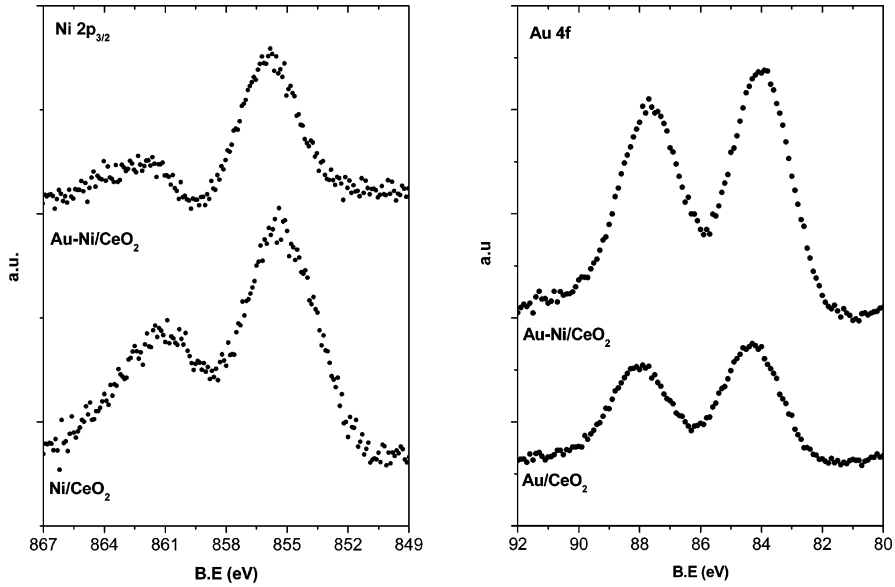

Figure 7. Comparative conventional XPS for Au/CeO_2, Ni/CeO_2, and $Au–Ni/CeO_2$ samples. Signals are normalized to Ce 3d and metallic charge obtained from ICP. The left panel shows the Ni $2p_{3/2}$ region, where the kinetic energy of the photoelectron is ∼600 eV. The right panel shows the Au 4f region, where the kinetic energy of the photoelectron is ∼1400 eV. Please note that the depth of analysis is much greater than in APPES.

compounds are generally detected at frequencies (2160−2130 cm^{-1}) lower than those of $CO–Ni^{2+}$ carbonyls, and they are much more stable.[34]

Conventional XPS and APPES. Figure 7 shows the XPS of the three catalysts (Au/CeO_2, Ni/CeO_2, and $Au–Ni/CeO_2$) corresponding to the Ni $2p_{3/2}$ and Au 4f regions. In the case of the Au 4f region, no major changes are observed between the two samples containing Au, and both spectra show a doublet with maxima at ∼84.0 eV, which is concordant with the presence of Au^0. In the case of Ni $2p_{3/2}$, the Ni/CeO_2 sample exhibits a peak at ∼855.4 eV and a well-defined satellite at ∼861.4 eV. The $Au–Ni/CeO_2$ sample also exhibits these two features, although the intensity of the satellite at ∼861.4 eV is much lower. The Ni 2p peak is a complex structure because of multiplet contributions and satellite structures at higher binding energies with respect to the main peak. A detailed explanation of the processes involving the appearance of this satellite can be found in recent papers.[37,38] In principle, the presence of a satellite at ∼6.0 eV can be assigned to a final effect peak associated with a (core)$3d^8L$ configuration (L being the ligand). Although the intensity (and position) of this satellite depends of many factors such as covalency with ligands, symmetry, particle size, and crystallinity, in a simplified scheme, all of these factors can reflect the different filling of the empty Ni 3d levels.

Figure 8 shows the ambient-pressure photoelectron spectroscopy (APPES) spectra for the $Au–Ni/CeO_2$ sample obtained in the presence of O_2 gas after H_2 treatment at 523 K. As explained in the Experimental Section, spectra were acquired using appropriated photon energy to yield the same kinetic energy for photoelectrons of Au 4f and Ni 2p.

First, it is worth noting that under both gas atmospheres (O_2 and H_2) the results obtained were almost identical. As explained before, the CO/O_2 mixture was not introduced because of experimental limitations, and two different situations (oxidizing and reducing conditions) were selected instead. In the figure, two different spectra are shown, corresponding to the two different kinetic energies (200 and 600 eV) used for acquisition, although data have be plotted on the B.E. scale. With regard to data obtained for photoelectrons with 200 eV of kinetic energy, we can observe a broad peak centered at ∼856 eV, which can be ascribed to Ni^{2+}, but at this kinetic energy, no significant Au 4f signal could be detected. On the other hand, spectra recorded at a photoelectron kinetic energy of 600 eV, where the analyzed thickness is estimated to be ∼3−4 nm, both Ni 2p (centered at 856 eV) and Au 4f (with the main peak of the doublet at 84.0 and 88.0 eV for Au $4f_{7/2}$ and Au $4f_{5/2}$, respectively) signals are observed.

It should also be mentioned that in this case the Ni 2p signal is significantly smaller than in the case of 200 eV of kinetic energy. Also, it is worth mentioning that the observed positions of Ni 2p and Au 4f signals are concordant with those expected for Ni^{2+} and Au^0. Nevertheless, it should remarked that the assignment of an "oxidation state" based on the binding energy of the Ni 2p signal is very complicated, because of, among some other factors, its broad full width at half-maximum and the small change in its position between ionized Ni states (Ni^{3+}, Ni^{2+}, and Ni^{+}), and therefore, oxidation states such as $Ni^{(2-\delta)+}$ could not be discarded.

DISCUSSION

We have shown that using conventional schemes for nanoparticle synthesis and standard preparation methods for catalysts (incipient wetness impregnation), we are able to prepare nanostructured catalysts with controlled size and composition and a narrow size distribution of the active phase and, at the same time, a homogeneous distribution over the surface. It is important to remark that in the bimetallic case this method has resulted not only in a global 1/1 Au/Ni composition but also in an almost individual 1/1 composition for all the particles (see a complete discussion below). This is quite important for the comparison of the sample with the monometallic ones, ensuring the "distinct" characteristic of the first, and not only the average behavior of the monometallic systems.

dx.doi.org/10.1021/cs400293b | ACS Catal. 2013, 3, 2169−2180

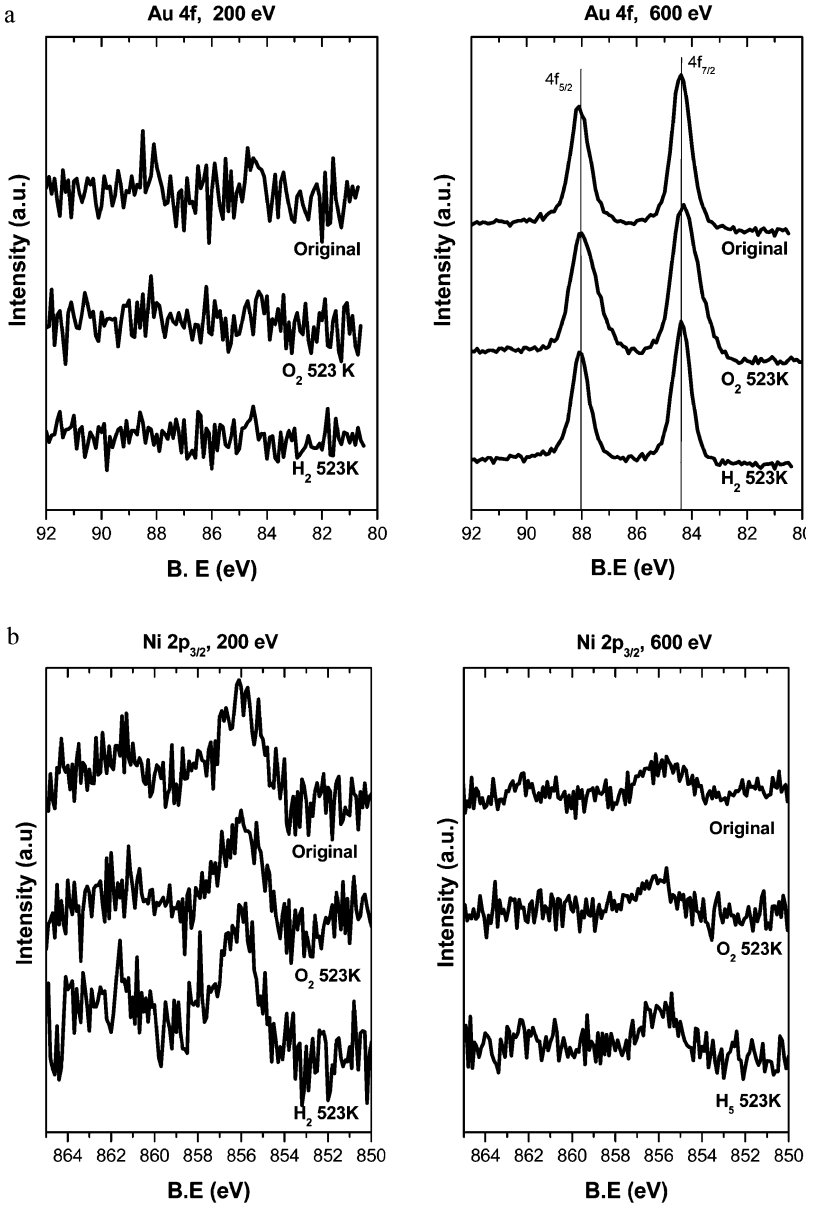

Figure 8. (a) Ambient-pressure photoelectron spectroscopy (APPES) spectra for the Au−Ni/CeO_2 sample obtained under "in operando" conditions. Original indicates O_2 and H_2 treatment at 723 K. Au 4f taken at 200 eV (left) and 600 eV (right) of photoelectron energy. (b) Ambient-pressure photoelectron spectroscopy (APPES) spectra for the Au−Ni/CeO_2 sample obtained under "in operando" conditions. Original indicates O_2 and H_2 treatment at 723 K. Ni $2p_{3/2}$ taken at 200 eV (left) and 600 eV (right) of photoelectron energy.

As revealed by SEM images and phase software analysis, particles of the active phase after deposition and calcination have a size that is almost double that of the original nanoparticles, in all the catalysts. This could suggest the prevalence of a coalescence mechanism in which a particle grows with the first "coordination sphere" (6+1) (see Figure 4 of the Supporting Information). In fact, it is well-known that nanoparticles obtained from these synthetic methods tend to arrange in a "Langmuir−Blodget" layer (see Figure 1), which is also true after deposition onto a support, as revealed previously by us.[39]

Besides the complete absence, after calcination treatment, of any contaminant from the capping layer and surfactant employed in the synthesis of the original NPs, combined data from conventional XPS and APPES give essential information about the distribution of the gold and Ni atoms on the bimetallic sample. In fact, the almost exclusive presence of Ni atoms on the surface of the catalyst nanoparticles is clearly revealed by the APPES spectra taken at 200 eV of kinetic energy (where only the Ni 2p signal is detected but not the Au 4f signal). The first implication of this result is that we cannot have particles showing gold atoms on its surface (or, at least, they have a very minor contribution). The spectra taken at 600 eV, on the other hand, reveal a clear Au 4f signal and a slightly weaker Ni 2p signal. Taking into consideration that for 200 eV of photoelectron energy, mean free path is ca. 0.6 nm and, therefore, we are analyzing ∼2 nm, but at 600 eV the analyzed depth is ∼4 nm, we can propose a model of bimetallic particles, with Ni atoms exclusively on the surface.

Keeping this model in mind, considering the relative atom sizes of Ni and Au, and assuming the observed 10 nm size for NPs particles in the calcined catalyst, we can propose a core−

dx.doi.org/10.1021/cs400293b | ACS Catal. 2013, 3, 2169−2180

shell structure with all the Ni atoms exposed with a shell thickness of ∼2 nm, and a core of the gold atoms of ∼8 nm (see Figure 9). This proposed model (calculus explained in more detail in the Supporting Information) with a shell with a 2 nm thickness and an 8 nm core (diameter) fits with the expected atomically derived volumes, taking into consideration gold and nickel atomic radii and a stoichiometry of 1/1. Furthermore, if we consider this model, with a shell of ∼1.2 nm composed of NiO, we could explain that with APPES results at 200 eV of photoelectron energy no gold atoms are detected, while these are observed when greater depth of analysis is considered (using 600 eV photoelectrons), as reflected in Figure 10.

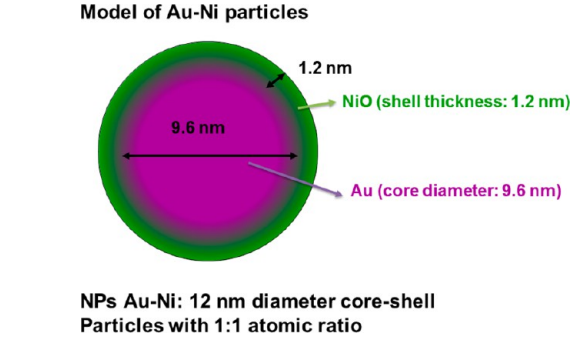

Figure 9. Proposed core−shell model of Au@Ni NPs in the Au−Ni/CeO_2 sample, considering the relative atom sizes of Ni and Au and assuming an observed size of 12 nm.

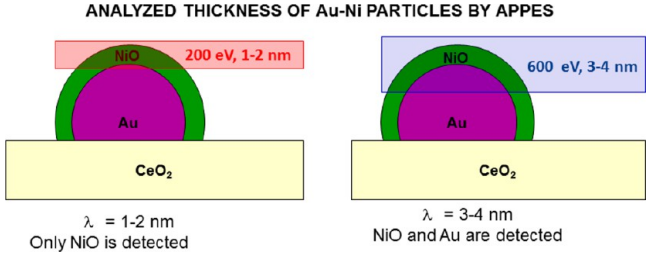

Figure 10. Scheme of approximated depth analysis of APPES for spectra taken at 200 and 600 eV of photoelectron energy and signals expected considering the particle size and distribution of Figure 9.

Comparison of reactivity data also provides important information. Thus, Au/CeO_2 catalysts exhibit better catalytic performance, as expected, than the Ni/CeO_2 sample. On the other hand, the Au−Ni/CeO_2 sample exhibits not only a better performance than the Ni/CeO_2 sample but also a better performance than the Au/CeO_2 sample. This is quite striking, because as we have discussed previously, for Au−Ni/CeO_2 under reaction conditions only nickel atoms are exposed on the surface (forming the shell of the nanoparticles), but those atoms present a modified reactivity with respect to Ni atoms of the Ni/CeO_2 sample. Therefore, we believe that Au atoms in the core of the Au@Ni nanoparticles induce an electronic effect on the local density of Ni d states via the presence of core Au atoms, similar to that proposed for Au−Ni surface alloys.[11,12] This electronic effect would be responsible for the modified chemical and reactivity properties of such particles, with a downshift in the T_{50} of the CO oxidation curves. As exposed in the Introduction, electronic effects has been proposed and probed by several techniques on bimetallic Au−Ni samples. On the other hand, there are few references for which that effect has a direct relation to an enhancement of the reactivity of the samples. Although Chin et al.[23] reported that in the case of bimetallic catalysts there is a lower level of coke formation, that could be the result of a geometric effect, because it is well-known that in Ni catalysts coke formation is favored with Ni particle size,[40,41] reflecting the fact that a minimal ensemble of Ni atoms is needed to induce coke formation. In this context, the reaction used in this work does not depend on those geometric effects, and the peak found by FTIR after adsorbing CO on the bimetallic sample reinforces the hypothesis that, in our case, the enhancement of reactivity is caused by a promotional effect caused by charge transfer. The FTIR peak position of the Au−Ni sample lies on an intermediate position between the CO−Ni^{2+} stretching band and the CO−Au^0 band, reflecting an electronically induced effect, although the DRIFTS data do not allow us to discern if the new CO band is originated by the adsorption on $Ni^{(2-\delta)+}$ atoms (it lies at wavenumbers lower than that of the CO−Ni^{2+} band) or on the CO−$Au^{\delta+}$ band (appears at a wavenumber higher than that of the CO−Au^0 band). In this context, it should be noted if we consider the shift experienced by the CO−metal band, this corresponds formally to an enrichment of the electronic density of the d band of the Ni atoms caused by an electronic transfer from core Au atoms. Although Au is more electronegative (in Pauling's concept) than Ni, and therefore such electron transfer should not occur, the situation is completely different when Ni^{2+}/Au^0 is considered. In that case, Ni^{2+} atoms could be considered to be more electronegative than Au^0 and, then, as acceptors of electrons from Au^0, resulting in a shift toward lower wavenumbers in DRIFTS CO−metal stretching vibration bands. Again, the evidence provided by other authors[23] that reflects the electronic transfer from gold atoms to $Ni^{(2-\delta)+}$ atoms reinforces this hypothesis. Although this shift in the DRIFTS wavenumber does not represent clear evidence of the electronic transfer from gold atoms to Ni^{2+} on its own, there are two other effects that reflect a change in the occupancy of the Ni3d levels, namely, the decrease in the satellite of the XPS Ni $2p_{3/2}$ spectrum of the Au−Ni/CeO_2 sample (at 864.1 eV) and the decrease in the intensity of the white line observed in the XANES spectrum of the Au−Ni/CeO_2 sample. Once more, it should be noted that probably each of these data can be understood with a different explanation but altogether fit with the proposed electronic transfer from Au atoms to NiO, yielding surface $Ni^{(2-\delta)+}$ species.

Alternatively, it would be possible to associate these changes in the reactivity with the presence of a SMSI effect. In fact, it is well-known that CeO_2 is a support that could present a SMSI effect on different metals such as Rh, Pt, and Ni,[42] greatly affecting its chemisorptive properties of H_2 or CO. Moreover, we have recently published an article in which we showed that besides other electronic effects, there is also a burial and flattening of Ni particles into the CeO_2 particles. Nevertheless, in both classical and more recent articles, it has been well established that this effect is normally associated with reduction at "high" temperatures (∼723−773 K), while calcination (even at high temperatures) or reduction under milder conditions does not induce such an SMSI effect. In the study presented here, samples have been treated in hydrogen only up to 523 K, a temperature too low to induce a SMSI effect. Moreover, it is also worth mentioning that, after that treatment, Ni remains oxidized (Ni^{2+}), discarding any SMSI effect. Nevertheless, if these samples were reduced at higher temperatures (∼773 K),

dx.doi.org/10.1021/cs400293b | ACS Catal. 2013, 3, 2169−2180

and on the basis of previous papers and our own research, we think that most probably there would be both electronic and geometric SMSI on these samples.[28]

It is also worth discussing why NiO is located on the surface of the particles. On metallic M1−M2@support systems, it has been proven that several factors constitute the driving force that drives one of the metals to the surface. The main factor is the surface energy of the metals (or oxides) involved in the core@shell particle. In principle, that metal (oxide) with the lower surface energy would tend to be in the shell of the particle.[43,44] Nevertheless, some other factors such as interaction with chemisorbed molecules (such as CO, used here) should be taken into account because recent work[45] has proven that Ni atoms on a Ni@Au sample tend to diffuse into the surface because of the driving force of the new Ni−CO bond formed. It is also worth noting that DFT calculations[46]and experimental results[47] have demonstrated that this diffusion is not kinetically limited even at room temperature.

CONCLUSIONS

Mono- and bimetallic Au−Ni nanoparticles have been prepared by conventional colloid recipes by high-temperature reduction of metal complexes with control of the size and composition of these NPs. In the case of bimetallic Au−Ni NPs, all the particles presented a 1/1 Ni/Au composition. APPES results indicate that at 200 eV of photoelectron energy, the contribution of gold is small, indicating that there are probably few individual Au nanoparticles. A similar conclusion can be drawn with DRIFTS and pure Ni nanoparticles.

Using simple and conventional methods of catalyst preparation (i.e., impregnation by incipient humectation), we have successfully deposited those NPs onto cerium oxide with control over the size distribution. Nevertheless, we have observed a significant increase in the size of the original particles after calcination, probably caused by the coalescence of the central+neighbor particles (6+1) coming from a compact two-dimensional arrangement of these as in a Langmuir−Blodget scheme. Nevertheless, this coalescence, via the calcination treatment in air at 773 K, is able to remove all the organics used as protective "capping" of NPs in their colloidal state before their deposition onto the CeO_2 support.

Taking into consideration the size of the particles, the relative atomic size of Ni and Au, the composition of the bimetallic particles (1/1 Au/Ni), and the APPES data, we could establish, based on the spectra taken at 200 and 600 eV of photoelectron energy and their corresponding IMFP, a core−shell distribution, in which Ni atoms are exposed on the shell and Au atoms in the core.

These Ni atoms exposed on the shell of the particles present modified chemical and reactivity properties, with a downshift in the T_{50} of the CO oxidation curves with respect to those of Ni and Au samples. This modified reactivity is caused by Au atoms in the core of the Au@Ni nanoparticles, which induces an electronic effect on the local density of Ni^{2+} d states. The latter effect, previously reported for model systems, is now reported for real catalysts. Recall the finding that these improved Au@Ni/CeO_2 catalysts have 50% of the Au atoms replaced by a much cheaper metal (Ni), which represents an important economic benefit. More efforts to prepare these type of smaller bimetallic catalysts are expected to induce a further improvement in the reactivity of these systems. In addition, the effect of reducing−oxidizing treatments on these core@shell-supported nanoparticles is expected to greatly affect these electronic effects and, hence, the reactivity of those catalysts.

ASSOCIATED CONTENT

Supporting Information

Additional data and figures and an explanation of the calculations used here. This material is available free of charge via the Internet at http://pubs.acs.org.

AUTHOR INFORMATION

Corresponding Author

*E-mail: jp.holgado@csic.es. Fax: (+34)954 460665.

Notes

The authors declare no competing financial interest.

REFERENCES

(1) Haruta, M. *Catal. Today* **1997**, *36* (1), 153−166.
(2) Bowker, M.; Nuhu, A.; Soares, J. *Catal. Today* **2007**, *122* (3−4), 245−247.
(3) Moreau, F.; Bond, G. C. *Catal. Today* **2007**, *122* (3−4), 260−265.
(4) Hidalgo, M.; Murcia, J.; Navío, J.; Colón, G. *Appl. Catal., A* **2011**, *397* (1), 112−120.
(5) Le Bars, J.; Specht, U.; Bradley, J. S.; Blackmond, D. G. *Langmuir* **1999**, *15* (22), 7621−7625.
(6) Della Pina, C.; Falletta, E.; Prati, L.; Rossi, M. *Chem. Soc. Rev.* **2008**, *37* (9), 2077−2095.
(7) Corma, A.; Garcia, H. *Chem. Soc. Rev.* **2008**, *37* (9), 2096−2126.
(8) Bracey, C. L.; Ellis, P. R.; Hutchings, G. J. *Chem. Soc. Rev.* **2009**, *38* (8), 2231−2243.
(9) Nielsen, L. P.; Besenbacher, F.; Stensgaard, I.; Laegsgaard, E.; Engdahl, C.; Stoltze, P.; Jacobsen, K. W.; Norskov, J. K. *Phys. Rev. Lett.* **1993**, *71* (5), 754−757.
(10) Jacobsen, J.; Nielsen, L. P.; Besenbacher, F.; Stensgaard, I.; Laegsgaard, E.; Rasmussen, T.; Jacobsen, K. W.; Norskov, J. K. *Phys. Rev. Lett.* **1995**, *75* (3), 489−492.
(11) Kratzer, P.; Hammer, B.; Norskov, J. K. *J. Chem. Phys.* **1996**, *105* (13), 5595−5604.
(12) Holmblad, P. M.; Larsen, J. H.; Chorkendorff, I.; Nielsen, L. P.; Besenbacher, F.; Stensgaard, I.; Laegsgaard, E.; Kratzer, P.; Hammer, B.; Norskov, J. K. *Catal. Lett.* **1996**, *40* (3−4), 131−135.
(13) Lahr, D. L.; Ceyer, S. T. *J. Am. Chem. Soc.* **2006**, *128* (6), 1800−1801.
(14) Winnischofer, H.; Rocha, T. C.; Nunes, W. C.; Socolovsky, L. M.; Knobel, M.; Zanchet, D. *ACS Nano* **2008**, *2* (6), 1313−1319.
(15) Xia, Y. N.; Xiong, Y. J.; Lim, B.; Skrabalak, S. E. *Angew. Chem., Int. Ed.* **2009**, *48* (1), 60−103.
(16) Semagina, N.; Kiwi-Minsker, L. *Catal. Rev.* **2009**, *51* (2), 147−217.
(17) Malet, P.; Caballero, A. *J. Chem. Soc., Faraday Trans. 1* **1988**, *84* (7), 2369−2375.
(18) Ogletree, D. F.; Bluhm, H.; Lebedev, G.; Fadley, C.; Hussain, Z.; Salmeron, M. *Rev. Sci. Instrum.* **2002**, *73*, 3872.
(19) Teschner, D.; Pestryakov, A.; Kleimenov, E.; Hävecker, M.; Bluhm, H.; Sauer, H.; Knop-Gericke, A.; Schlögl, R. *J. Catal.* **2005**, *230*, 186.
(20) Ogletree, D. F.; Bluhm, H.; Hebenstreit, E. D.; Salmeron, M. *Nucl. Instr. Meth. Phys. Res. A* **2009**, *601* (1−2), 151−160.
(21) Holgado, J. P.; Alvarez, R.; Munuera, G. *Appl. Surf. Sci.* **2000**, *161* (3−4), 301−315.
(22) González-Elipe, A. R.; Alvarez, A.; Holgado, J. P.; Fernandez, A.; Espinós, J. P.; Munuera, G. In *Fundamental Aspects of Heterogeneous Catalysts by Particle Beams*; Brongersma, H. H., Van Santen, R. A., Eds.; Plenum: New York, 1991; Vol. *265*, pp 227−235. Gonzalezelipe, A. R.; Espinos, J. P.; Fernandez, A.; Munuera, G. *J. Catal.* **1991**, *130* (2), 627−641.

(23) Chin, Y. H.; King, D. L.; Roh, H. S.; Wang, Y.; Heald, S. M. *J. Catal.* **2006**, *244* (2), 153−162.
(24) Johnson, M. F. L.; Mooi, J. *J. Catal.* **1987**, *103* (2), 502−505.
(25) Johnson, M. F. L.; Mooi, J. *J. Catal.* **1993**, *140* (2), 612−612.
(26) Tournayan, L.; Marcilio, N. R.; Frety, R. *Appl. Catal.* **1991**, *78* (1), 31−43.
(27) Trovarelli, A.; Dolcetti, G.; Deleitenburg, C.; Kaspar, J.; Finetti, P.; Santoni, A. *J. Chem. Soc., Faraday Trans.* **1992**, *88* (9), 1311−1319.
(28) Holgado, J. P.; Munuera, G. XPS/TPR study of the reducibility of M/CeO_2 catalysts (M = Pt, Rh): Does junction effect theory apply? In *Catalysis and Automotive Pollution Control III*; Frennet, A., Bastin, J. M., Eds.; Elsevier: Amsterdam, 1995; Vol. *96*, pp 109−122.
(29) Yamada, T.; Kayano, K.; Funabiki, M. *Stud. Surf. Sci. Catal.* **1993**, *77*, 329−332.
(30) Yao, H. C.; Yao, Y. F. Y. *J. Catal.* **1984**, *86* (2), 254−265.
(31) Manzoli, M.; Chiorino, A.; Vindigni, F.; Boccuzzi, F. *Catal. Today* **2012**, *181* (1), 62−67.
(32) Zafiris, G. S.; Gorte, R. J. *J. Catal.* **1993**, *139* (2), 561−567.
(33) Huang, X. S.; Sun, H.; Wang, L. C.; Liu, Y. M.; Fan, K. N.; Cao, Y. *Appl. Catal., B* **2009**, *90* (1−2), 224−232 and references therein.
(34) Hadjiivanov, K. I.; Vayssilov, G. N. In *Advances in Catalysis*; Gates, B. C., Knozinger, H., Eds.; Elsevier: Amsterdam, 2002; Vol. *47*, pp 307−511.
(35) Tkachenko, O. P.; Kustov, L. M.; Nikolaev, S. A.; Smirnov, V. V.; Klementiev, K. V.; Naumkin, A. V.; Volkov, I. O.; Vasil'kov, A. Y.; Murzin, D. Y. *Top. Catal.* **2009**, *52* (4), 344−350.
(36) Mihaylov, M.; Knozinger, H.; Hadjiivanov, K.; Gates, B. C. *Chem. Ing. Tech.* **2007**, *79* (6), 795−806.
(37) Hagelin-Weaver, H. A. E.; Weaver, J. F.; Hoflund, G. B.; Salaita, G. N. *J. Electron Spectrosc. Relat. Phenom.* **2004**, *134* (2−3), 139−171.
(38) Grosvenor, A. P.; Biesinger, M. C.; Smart, R. S. C.; McIntyre, N. S. *Surf. Sci.* **2006**, *600* (9), 1771−1779.
(39) Caballero, A.; Holgado, J. P.; Gonzalez-delaCruz, V. M.; Habas, S. E.; Herranz, T.; Salmeron, M. *Chem. Commun.* **2010**, *46* (7), 1097−1099.
(40) Trimm, D. L. *Catal. Today* **1997**, *37* (3), 233−238.
(41) Rostrup-Nielsen, J. R.; Sehested, J.; Norskov, J. K.. In *Advances in Catalysis*; Gates, B. C., Knozinger, H., Eds.; Elsevier: Amsterdam, 2002; Vol. *47*, pp 65−139.
(42) Zhuang, Q.; Qin, Y.; Chang, L. *Appl. Catal.* **1991**, *70* (1), 1−8.
(43) Ruban, A. V.; Skriver, H. L.; Norskov, J. K. *Phys. Rev. B* **1999**, *59* (24), 15990−16000.
(44) Maillet, T.; Barbier, J., Jr.; Gelin, P.; Praliaud, H.; Duprez, D. *J. Catal.* **2001**, *202* (2), 367−378.
(45) Tenney, S. A.; He, W.; Roberts, C. C.; Ratliff, J. S.; Shah, S. I.; Shafai, G. S.; Turkowski, V.; Rahman, T. S.; Chen, D. A. *J. Phys. Chem. C* **2011**, *115* (22), 11112−11123.
(46) Chandler, B. D.; Long, C. G.; Gilbertson, J. D.; Pursell, C. J.; Vijayaraghavan, G.; Stevenson, K. J. *J. Phys. Chem. C* **2010**, *114* (26), 11498−11508.
(47) Tao, F.; Grass, M. E.; Zhang, Y. W.; Butcher, D. R.; Renzas, J. R.; Liu, Z.; Chung, J. Y.; Mun, B. S.; Salmeron, M.; Somorjai, G. A. *Science* **2008**, *322* (5903), 932−934.